

# Dextran-Based Doxorubicin Nanocarriers with Improved Tumor Penetration

Sharon M. Sagnella,<sup>†,‡</sup> Hien Duong,<sup>†</sup> Alex MacMillan,<sup>§</sup> Cyrille Boyer,<sup>†</sup> Renee Whan,<sup>†,§</sup> Joshua A. McCarroll,<sup>†,‡</sup> Thomas P. Davis,<sup>||,⊥</sup> and Maria Kavallaris<sup>\*,†,‡</sup>

<sup>†</sup>Australian Centre for Nanomedicine and <sup>§</sup>Biomedical Imaging Facility, Mark Wainwright Analytical Centre, University of New South Wales, Sydney, Australia

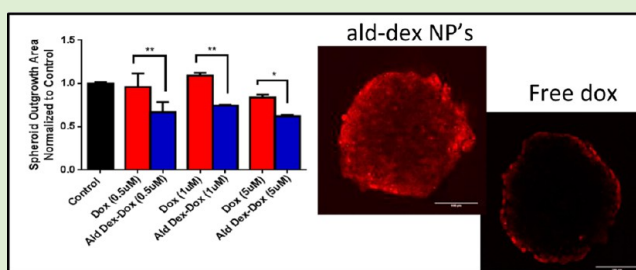
<sup>‡</sup>Children's Cancer Institute Australia, Lowy Cancer Research Centre, University of New South Wales, P.O. Box 81, Randwick, Australia

<sup>||</sup>Monash Institute of Pharmaceutical Sciences, Monash University, Parkville, Melbourne, Victoria, Australia

<sup>⊥</sup>Department of Chemistry, University of Warwick, Coventry, United Kingdom

## S Supporting Information

**ABSTRACT:** Drug delivery systems with improved tumor penetration are valuable assets as anticancer agents. A dextran-based nanocarrier system with aldehyde functionalities capable of forming an acid labile linkage with the chemotherapy drug doxorubicin was developed. Aldehyde dextran nanocarriers (ald-dex-dox) demonstrated efficacy as delivery vehicles with an IC<sub>50</sub> of ~300 nM against two-dimensional (2D) SK-N-BE(2) monolayers. Confocal imaging showed that the ald-dex-dox nanocarriers were rapidly internalized by SK-N-BE(2) cells. Fluorescence lifetime imaging microscopy (FLIM) analysis indicated that ald-dex-dox particles were internalized as intact complexes with the majority of the doxorubicin released from the particle four hours post uptake. Accumulation of the ald-dex-dox particles was significantly enhanced by ~30% in the absence of glucose indicating a role for glucose and its receptors in their endocytosis. However, inhibition of clathrin dependent and independent endocytosis and macropinocytosis as well as membrane cholesterol depletion had no effect on ald-dex-dox particle accumulation. In three-dimensional (3D) SK-N-BE(2) tumor spheroids, which more closely resemble a solid tumor, the ald-dex-dox nanoparticles showed a significant improvement in efficacy over free doxorubicin, as evidenced by decreased spheroid outgrowth. Drug penetration studies in 3D demonstrated the ability of the ald-dex-dox nanocarriers to fully penetrate into a SK-N-BE(2) tumor spheroids, while doxorubicin only penetrates to a maximum distance of 50 μM. The ald-dex-dox nanocarriers represent a promising therapeutic delivery system for the treatment of solid tumors due to their unique enhanced penetration ability combined with their improved efficacy over the parent drug in 3D.



## INTRODUCTION

Neuroblastoma, the most common extra-cranial childhood tumor, accounts for 6–10% of all childhood cancers and 15% of all pediatric oncology deaths. It has one of the lowest survival rates of all pediatric cancers, and ~50% of patients present with metastatic tumors conferring a poor prognosis.<sup>1–3</sup> Long-term survivors of the disease suffer lifelong health issues related to the highly toxic chemotherapeutics administered.<sup>4</sup> One such drug, doxorubicin, an antibiotic with broad spectrum antitumor activity in a variety of solid tumors including neuroblastoma, has a limited therapeutic index due to toxic side effects such as cardiotoxicity and myelosuppression combined with the inability of the drug to penetrate more than a few cell diameters into tumor tissue.<sup>5–7</sup> Thus, the ability to deliver chemotherapy drugs such as doxorubicin directly to the tumor site, while maintaining high efficacy combined with low systemic exposure represents the holy grail in terms of cancer treatments.

The exploitation of the unique properties of nanoscale and nanostructured materials in medical applications has been explored extensively as a promising strategy in the advancement of anticancer therapies with the ability to overcome many of the limitations common to conventional chemotherapeutic agents.<sup>8–10</sup> The naturally occurring polysaccharide dextran possesses a number of appealing characteristics from a drug delivery perspective and thus has been incorporated into a variety of nanoparticle formulations.<sup>11–15</sup> Dextran is neutrally charged and systems with no surface charge have been shown to experience reduced plasma protein adsorption and an increased rate of nonspecific cellular uptake.<sup>16</sup> Dextran is water-soluble and hydrophobically modified dextran forms micelles which can be used to either encapsulate drugs or be

Received: October 14, 2013

Revised: December 3, 2013

Published: December 9, 2013

functionalized with drugs via it is numerous hydroxyl groups.<sup>11,13,15,17–19</sup> Furthermore, dextran-drug conjugates have been shown to overcome drug resistance in P-glycoprotein overexpressing multidrug-resistant cells.<sup>12,17,19</sup>

Drug-loaded nanocarrier formulations including those containing dextran can exhibit improved pharmacokinetics and reduced systemic toxicity as compared to their parent drug as a result of passive targeting in which circulating drug nanocarriers deposit preferentially into tumor tissue due to the leaky vasculature often associated with these tumors (EPR effect).<sup>6,9,12,20</sup> However, passive targeting is highly influenced by not only the physicochemical properties of the particle system such as particle size, shape, and surface chemistry, but also tumor characteristics (size, location, vascularity, heterogeneity, etc.), and thus, passively targeted drug loaded nanocarriers have met with limited success due to an incomplete understanding of the tumor microenvironment and an over reliance on the EPR effect.<sup>9,21,22</sup>

Low penetration into the extravascular tumor tissue and limited access to tumor cells remains a major obstacle in the use of nanocarriers for the effective delivery of therapeutics throughout solid tumors.<sup>6,7,20,23</sup> Small molecular weight drugs and to a larger extent bulky nanoparticle systems are significantly hindered from penetrating deep into tumor tissue due to a variety of factors. First, the high variability in the leaky nature of the endothelium can restrict access to certain areas of the tumor.<sup>10</sup> Once nanoparticles have exited the vessels, they usually have to pass through additional cellular layers including smooth muscle cells and fibroblasts before gaining access to the tumor cells.<sup>10,24</sup> Interstitial pressure increases with increasing distance from the vessel further preventing nanoparticles from penetrating deeply into the tumor while the dense extracellular matrix presents an additional barrier with stiffer tumors more difficult to penetrate.<sup>6,10,24</sup> Finally, the high cell density of tumor cells are difficult to penetrate with most chemotherapy drugs only able to travel 3–5 cell diameters into the tumor and larger nanocarriers hindered to an even greater extent.<sup>10,24</sup> As most nanoparticle studies are conducted initially in two-dimensional (2D) cell monolayers where nanocarriers tend to show great promise, it is usually not until these systems are tested in animals or even preclinical trials that their inability to effectively access tumor cells in vivo is observed. The large discrepancy between nanocarrier behavior in vitro and in vivo combined with the fact that in vivo models are costly, complicated, and time-consuming highlights the necessity of employing 3D cell culture models for in vitro prescreening of nanoparticle delivery systems.

A handful of strategies have begun to emerge in an attempt to overcome the limited tumor penetration inherent in nanoparticle systems. These include the development of “multistage” nanoparticles designed to be broken down by tumor-associated proteases or enzymes into smaller nanoparticles or bioactive molecules following extravasation allowing them to effectively fully penetrate into the tumor as well as the attachment of peptides onto the nanocarrier surface with tumor penetrating properties.<sup>6,7,25,26</sup> Furthermore, shape and surface charge have been shown to effect tumor penetration, with negatively charged particles and those with a more cylindrical shape exhibiting enhanced penetration.<sup>10,27,28</sup> Finally, pretreatment or codelivery of nanoparticles with drugs, enzymes, or inflammatory mediators have also been implicated in enhancing intratumoral transport of nanoparticles.<sup>29,30</sup>

Despite these approaches, requirements for enhancing nanoparticle penetration is not well studied and, hence, is still poorly understood. Here, we report on a dextran based doxorubicin nanocarrier system with enhanced tumor penetration properties. Doxorubicin is linked to the nanocarrier by an acid labile bond capable of being cleaved in a low pH environment. These particles are successfully taken up by neuroblastoma cells followed by release of the doxorubicin inside the cell. Furthermore, the dextran-doxorubicin nanocarriers are capable of full penetration into neuroblastoma tumor spheroids with an average diameter of ~400–500  $\mu\text{m}$ , while free doxorubicin can only penetrate ~50  $\mu\text{m}$  into these structures. Due to this enhanced penetration, these nanocarriers display enhanced efficacy over free doxorubicin in 3D tumor spheroids. The ability to enhance penetration and more effectively deliver therapeutics into tumors overcomes one of the major obstacles in the development of highly effective nanocarriers.

## MATERIALS AND METHODS

**Synthesis of Aldehyde Functionalized Dextran by Oxidation of Dextran with Sodium Periodate.** The aldehyde-functionalized dextran derivative was synthesized by using the method of Bernstein et al.<sup>31</sup> Briefly, sodium periodate ( $\text{NaIO}_4$ ; 3.2 g, 0.015 mol) was dissolved in deionized water (100 mL). The solution was protected from light. After adding dextran (2.5 g,  $M_w$  10000 g/mol, from Leuconostocmesenteroides mmol) in the sodium periodate solution, the mixture was stirred overnight at room temperature in the dark. The product was extensively dialyzed against water to remove excess reactant using cellulose membrane (MWCO of 3500 g/mol). The purified aldehyde functionalized dextran was lyophilized to obtain a white powder for long-term storage (4.4 g).

**Synthesis of Aldehyde-Functionalized Dextran–Doxorubicin Conjugates with a Schiff Base Linkage and Formation of Nanoparticles in the Presence of PEG-Amine.** In the presence of triethylamine (50  $\mu\text{L}$ ), aldehyde-functionalized dextran (100 mg), and doxorubicin (dox; 10 mg) were dissolved in DMSO (2 mL) and the solution was stirred for 4 h, followed by the adding of the solution of PEG-amine (10 mg) in DMSO (1 mL). The mixture was stirred overnight at room temperature. Phosphate buffer solution (PBS, pH 7.4, 6 mL) was then added and the mixture was stirred at room temperature for 1 h. The mixture was first dialyzed (MWCO 11000 Da) against a DMSO and PBS (pH 7.4) mixture (1:9, v/v) for 24 h and then against PBS alone for 24 h to remove solvent, triethylamine, unreacted PEG-amine and free dox, before lyophilization yielding a red powder.

The final dox concentration in the aldehyde dextran doxorubicin conjugates (ald-dex-dox) was determined using UV–visible spectrophotometry ( $\lambda = 485 \text{ nm}$ ). After dissolving ald-dex-dox (1 mg) in DMSO (1 mL), the solution absorbance at 485 nm was measured on a CARY 300 spectrophotometer (Bruker). The amount of encapsulated dox in the dextran conjugate was quantified to be 4.5 wt % using a calibration curve of dox-HCL in DMSO. Due to the amphiphilic nature of the synthesized dextran doxorubicin polymer conjugate, polymer micelles were formed via self-assembly upon addition of water.

**Release of Doxorubicin from Aldehyde-Functionalized Aldehyde Dextran Doxorubicin Conjugates.** The release rate of dox from ald-dex-dox nanoparticles was carried out in vitro in acetate buffer (pH 5.0 to mimic the pH conditions of endosomes and lysosomes) and phosphate buffer (pH 7.0). The nanoparticle solution after dialysis (2 mL, 1 mg  $\text{mL}^{-1}$ , 4.5% of dox) was placed in a dialysis membrane tube (MWCO 3500 Da), prior to immersion in 50 mL of acetate buffer (pH 5.0) or phosphate buffer (pH 7.0). The bottles were covered with aluminum foil and placed in a shaking incubator with stirring speed of 100 rpm at 37 °C. At specific time intervals (1–7 days), 3 mL of the media were taken for doxorubicin concentration analysis. Equal volume of fresh media was replaced and the sink

condition, where dox concentrations in the release medium were below 10% of its aqueous solubility (2.1 mg/mL), was maintained during the course of the release study.<sup>32</sup> Dox was determined using fluorescence spectroscopy at the emission wavelength of 560 nm, excitation wavelength of 480 nm, and slit width of 10 nm. The release experiments were conducted in triplicate and the result is presented as an average of these three values.

**Nuclear Magnetic Resonance (NMR).** Structures of the synthesized compounds were analyzed by <sup>1</sup>H NMR spectroscopy using a Bruker DPX 300 spectrometer at 300 MHz for hydrogen nuclei.

**Gel Permeation Chromatography (GPC) Measurements.** DMAC GPC analyses of the polymers were performed in *N,N*-dimethylacetamide [DMAC; 0.03% w/v LiBr, 0.05% 2,6-dibutyl-4-methylphenol (BHT)] at 50 °C (flow rate = 1 mL·min<sup>-1</sup>) using a Shimadzu modular system comprised of an SIL-10AD autoinjector, a PL 5.0-mm bead-size guard column (50 × 7.8 mm) followed by four linear PL (Styragel) columns (10<sup>5</sup>, 10<sup>4</sup>, 10<sup>3</sup>, and 500 Å) and a RID-10A differential refractive-index detector. The SEC calibration was performed with narrow-polydispersity polystyrene standards ranging from 500 to 10<sup>6</sup> g·mol<sup>-1</sup>. A total of 50 μL of polymer solution (2 mg·mL<sup>-1</sup> in DMAC) was injected each time, for analysis.

**UV-Visible Spectroscopy.** UV-visible spectra were recorded using a CARY 300 spectrophotometer (Bruker).

**Fluorescence Spectroscopy.** The fluorescence spectra of dox and ald-dex-dox nanoparticles in aqueous solutions were collected using a Cary Eclipse Spectrophotometer. The fluorescence spectra were recorded in the range of 500–650 nm by excitation at 485 nm with slits of 10 nm.

**Dynamic Light Scattering (DLS).** DLS measurements were performed using a Malvern Zetasizer Nano Series running DTS software and using a 4 mW He–Ne laser operating at a wavelength of 633 nm and an avalanche photodiode (APD) detector. The scattered light was detected at an angle of 173°. The temperature was stabilized to ±0.1 °C of the set temperature. To reduce the influence of larger aggregates the number-average hydrodynamic particle size is reported. The dispersity index is used to describe the width of the particle size distribution, as calculated from the DTS software using a cumulant analysis of the measured intensity autocorrelation function; it is related to the standard deviation of the hypothetical Gaussian distribution (i.e., dispersity =  $s^2/Z_D^2$ , where  $s$  is the standard deviation and  $Z_D$  is the  $Z$  average mean size).

**Transmission Electron Microscopy (TEM).** The sizes and morphologies of nanoparticles were observed using a transmission electron microscopy JEOL1400 TEM at an accelerating voltage of 100 kV. The particles were dispersed in water (1 mg/mL) and deposited onto a 200 mesh, holey film, copper grid (ProSciTech). Osmium vapor (OsO<sub>4</sub>) staining was applied.

**Cell Culture.** Human neuroblastoma cell lines SH-SY-5Y, SK-N-BE(2), and SK-N-BE(2) cells expressing the SFG-NESTGL triple-modality reporter construct containing the green fluorescent protein (GFP) and firefly luciferase genes (SK-N-BE(2)/TGL),<sup>33</sup> as well as the normal fetal lung fibroblasts MRC-5, were grown in monolayers in Dulbecco's Modified Eagle Media (DMEM; Gibco-Invitrogen) containing 10% FCS and maintained in culture at 37 °C in a humidified atmosphere containing 5% CO<sub>2</sub> and were routinely screened and found to be free of mycoplasma. Cells were passaged 2–3 times per week using phosphate buffered saline (PBS)/Trypsin.

Tumor spheroids of either SK-N-BE(2) or SK-N-BE(2)/TGL cells were generated in 96-well round-bottom plates (Sigma-Aldrich), as previously published.<sup>34</sup> Spheroids with an average diameter of ~400–500 μm after 4 days growth were used for nanoparticle penetration studies.

**Cell Viability in Monolayers.** The cytotoxicity of dox, ald-dex-dox, and acetylated dextran micelles physically loaded with dox (ac-dex-dox) were tested in vitro in monolayers via a cellular metabolic activity (cell proliferation) assay in which a resazurin solution was added to triplicate wells. The cells were seeded at 10000 cells/well for SH-SY-5Y, 5000 cells/well for MRC5, and 1250 cells/well for SK-N-BE(2)/TGL in 96-well tissue culture plates and incubated for 24 h.

The medium was then replaced with fresh medium containing dox, ald-dex-dox, or ac-dex-dox over an equivalent dox concentration range of 0.001–50 μM. At 72 h post drug/particle incubation, treatments were removed and fresh media was added (100 μL) followed by the addition of the resazurin solution (20 μL) to each well and the cells were incubated for 6 h and absorbance measured using a Benchmark Plus microplate spectrophotometer reader (Biorad) at 570 nm (595 nm reference wavelength). Cell viability was determined as a percentage of untreated control cells, and IC<sub>50</sub> values were calculated via regression analysis using Graphpad Prism 5.

**Cell Viability in Spheroids.** The toxicity of dox and chemically linked ald-dex-dox was assessed in spheroids via a Trypan Blue exclusion assay. After 4 days growth, spheroids with an average diameter of ~400–500 μm were either left untreated or treated with dox or ald-dex-dox at three different equivalent dox concentrations (0.25, 0.5, and 1 μM) for 24 h. Spheroids and media were harvested and disaggregated via trypsinization followed by pipetting to obtain a single cell suspension. Dead cells were identified using 0.4% trypan blue stain (Invitrogen). Cell counts were obtained by counting the number of live cells/96 spheroids. Percentage cell viability was determined by dividing the total number of live cells by the total number of cells (live + dead).

**Spheroid Outgrowth Assay.** After 4 days growth, spheroids with an average diameter of ~400–500 μm were either left untreated or treated with dox or ald-dex-dox at three different equivalent dox concentrations (0.5, 1, and 5 μM) for 4 h. After 4 h treatment, spheroids were washed thoroughly to remove any remaining drug in the media and then transferred to 6 well tissue culture plates. Spheroids were left to attach and grow out on the plates for 24 h. After 24 h, images were obtained and outgrowth quantified using the AxioVision software package.

**Spheroid Penetration.** Analysis of spheroid penetration was done in Image J. Images acquired 100 μm from the bottom of the spheroid were converted to surface plots and a 1D fluorescence intensity profile was taken by drawing a across the plot from edge to edge. A total of 5 to 6 spheroids were analyzed per treatment per time point and averaged to produce the penetration depth profile.

**Doxorubicin Extraction from Nuclear Fraction.** SK-N-BE(2) cells were grown in monolayers in T75 flasks to ~40% confluence and then incubated with dox or ald-dex-dox at 0.5 μM equivalent dox concentration for 4, 24, 48, or 72 h. Cells were then harvested by trypsinization and counted to obtain at least 5 × 10<sup>6</sup> cells for extraction. Following centrifugation at 1500 rpm for 3 min, media was removed and 500 μL of lysis buffer (100 mM NaCl, 1 mM EDTA, 1% triton-X, 10 mM Tris buffered saline) was added to the cells. Cells were lysed for 10 min at 4 °C, and the suspension was centrifuged at 800g for 15 min/4 °C. The supernatant containing the cytoplasmic fraction was removed and 200 μL of acidified ethanol (0.3 N HCL + EtOH) was added to the nuclear fraction and vortexed briefly to resuspend. Doxorubicin was extracted from the nuclear fraction for 24 h at 4 °C. The extracted fraction was centrifuged at 3000g for 5 min and 20 μL of the supernatant was placed into a well of a black 384-well plate. Fluorescence was measured using a Victor plate reader (Perkin-Elmer, Waltham, U.S.A.) excitation 488/emission 590. Extraction from the nuclear fraction of untreated cells was subtracted as background, and μg dox/10<sup>6</sup> cells was calculated from a standard curve created with set concentrations of dox or ald-dex-dox in acidified ethanol.

**Endocytosis Inhibitors.** To examine different endocytic routes of ald-dex-dox particle uptake, cells were incubated for 2 h in Opti-MEM containing one of the following inhibitors: 5 μg/mL chlorpromazine (clathrin dependent), 400 μM genistein (clathrin independent), 1.25 μM methyl β-cyclodextrin (clathrin independent), or 50 μM 5-(*N*-ethyl-*N*-isopropyl)amirolide (EIPA, macropinocytosis). Cells were then rinsed 2× with PBS and treated with 0.5 μM equivalent dox concentration for 1 h prior to examination via flow cytometry or confocal microscopy.

**Sugar Inhibition.** Cells were incubated in either RPMI containing serum and glucose, RPMI containing serum and no glucose, or RPMI with no glucose and no serum for 24 h. After 24 h, cells were treated with 0.5 μM equivalent dox concentration of dex-dox particles and



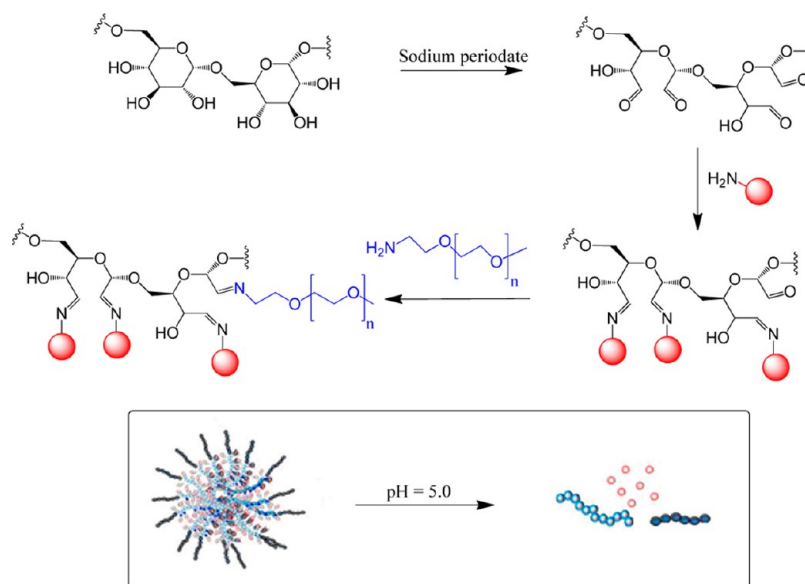


**Figure 1.** Oxidation of dextran polymers with sodium periodate: Schematic representation of PEG and dox conjugated to dextran polymers to yield PEG/dox dextran nanoparticles.

incubated for 1 h. Additionally, cells incubated in normal DMEM media were treated with a combination of  $0.5 \mu\text{M}$  equiv dox of dex-dox particles and  $5 \mu\text{g/mL}$  concanavalin A for 1 h prior. Uptake of dex-dox particles was examined via flow cytometry.

**Flow Cytometry.** For analysis via flow cytometry, SK-N-BE(2) cells were plated at 200000 cells/well in six-well tissue culture plates and left to grow for 24 h. Cells were harvested via trypsinization, resuspended in  $500 \mu\text{L}$  of PBS, and collected into 5 mL of polystyrene round-bottom Falcon tubes ( $12 \times 75 \text{ mm}$ ). A FACSCanto flow cytometer (Becton-Dickinson) equipped with BD Biosciences FACSDiva Software was used for detection of doxorubicin fluorescence intensity. Data shown represents the PerCP geometric mean for 10000 events as analyzed using the FlowJo software.

**FLIM.** FLIM measurements were acquired using a Picoquant Microtime200 inverted confocal microscope with a  $63\times 1.2 \text{ NA}$  water-immersion objective. Dox was excited using 550 nm diode laser at a repetition rate of 40 MHz. Fluorescence emission was detected 550 nm long-pass filter using a single-photon avalanche diode (SPAD) and PicoHarp300 TCSPC electronics. Fluorescein was used to calibrate the phasor plot to a monoexponential lifetime of 4 ns. Phasor analysis was performed using simFCS (developed by Enrico Gratton, Laboratory of Fluorescence Dynamics, Irvine, CA).

**Confocal Microscopy.** Cells (5000 cells/dish) were plated in 35 mm cultured dishes which were precoated with poly-D-lysine hydrobromide for 10 min and left to grow for 3 days. Two types of confocal microscopes, Zeiss LSM 780 and Leica TCS SP5, were utilized to acquire images, both equipped with an environmental chamber which controls the atmospheric conditions, humidity, and temperature for live-cell imaging. Monolayer images were acquired on the Leica TCS SP5 with using a  $63\times 1.4 \text{ NA}$  Leica oil objective. The Zeiss LSM 780 was equipped with multiple laser lines for fluorescence measurements and a  $63\times 1.3 \text{ NA}$  water/glycerol objective was used for imaging monolayers. Spheroids were imaged using the  $10\times 0.45 \text{ NA}$  and  $20\times 0.8 \text{ NA}$  air objectives. Hoechst 33342 was used as a nuclear counterstain.

**Statistics.** All statistical analysis was performed using the Graphpad Prism software package. Data is represented as mean  $\pm$  standard deviation. Statistical significance between groups was determined by a one way ANOVA, followed by the Tukey's multiple comparison test.  $\text{IC}_{50}$  was determined via regression analysis. Statistical significance of penetration curves was determined by two-way ANOVA.

## RESULTS AND DISCUSSION

### Synthesis and Characterization of Doxorubicin-Loaded Aldehyde-Functionalized Nanoparticles.

Dextran is an appealing starting material to make nanoparticles for bioapplications as it is biodegradable and approved for in vivo use as a plasma expander.<sup>35</sup> Many studies have shown that dextran can be easily functionalized with biomolecules or drugs via its hydroxyl groups either by direct esterification or by the preintroduction of spacer arms.<sup>11,13,14,36,37</sup> The dextran polymer contains an abundance of hydroxyl groups on glucose monomer units. These hydroxyl group may be oxidized with sodium periodate to cleave the associated carbon–carbon bonds and produce two aldehyde groups per glucose moiety (Figure 1).<sup>31</sup> The presence of aldehyde functionality was confirmed by  $^1\text{H}$  NMR analysis with the appearance of a new signal at  $\delta = 9.7 \text{ ppm}$  attributed aldehyde proton (Figure S1).

Dox can be conjugated to aldehyde group functionalized dextran polymers under mild conditions resulting in the formation of Schiff base (imine bonds). The addition of acid catalyzes the back-reaction in the presence of water to reform the aldehyde group, and provides a facile mechanism for the release of a drug. This pH sensitivity property, which has been used in other nanoparticle formulations,<sup>11,13</sup> is useful for drug delivery applications as the targeted areas for therapy are often mildly acidic (such as endosome/lysosome compartments and the tumor microenvironment). Following conjugation with dox, amphiphilic-like polymers form which can self-assemble in aqueous solution to form micelles. Following purification, doxorubicin-conjugated dextran was analyzed by UV–visible and  $^1\text{H}$  NMR analysis.  $^1\text{H}$  NMR displayed a decrease in the intensity of the aldehyde signal at 9.7 ppm, while UV–visible spectroscopy confirmed the attachment of dox by the presence of a signal at 495 nm. The drug content was determined to be 4.5 wt % ( $\pm 0.2\%$ ) using a calibration curve, while the conjugation yield was over 90% (Figures S2 and S3). The morphology of self-assembled aggregates of the dox conjugated aldehyde dextran was investigated using dynamic light scattering (DLS) and transmission electron microscopy (TEM). TEM (Figure S4) showed the formation of large

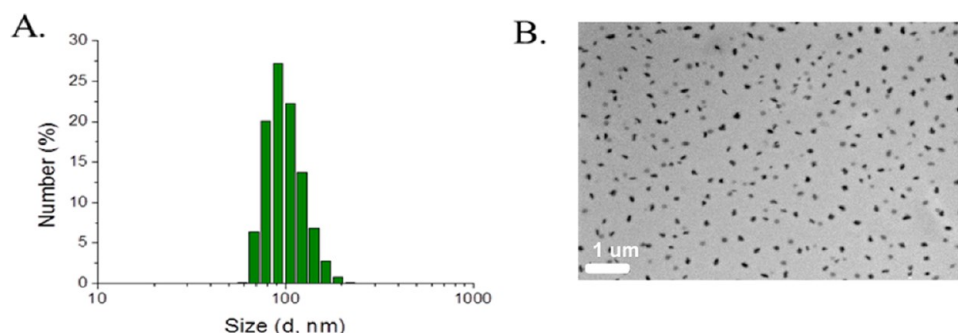


**Figure 2.** (A) Dynamic light scattering (DLS) of dox conjugated to the dextran nanoparticles in water (concentration 1 mg/mL). (B) TEM image of PEG and dox conjugated to dextran nanoparticles (ald-dex-dox).

aggregates ( $\sim 100$ – $500$  nm), which was in good agreement with DLS analysis ( $\sim 300 \pm 50$  nm; with a broad dispersity 0.4). However, because these particles were observed to degrade in water and precipitate after a few hours, short PEG-NH<sub>2</sub> ( $M_w = 5000$  g/mol) was introduced to increase stability and solubility. To do so, PEG-amine chains which could react with residual aldehyde groups were added to dox conjugated aldehyde functionalized dextran (Figure 1). The nanoparticles were purified by dialysis for 24 h and then characterized by UV–visible spectroscopy, TEM, and DLS. TEM showed uniform nanoparticles  $\sim 100$  nm in size, consistent with DLS analysis (Figure 2). Additionally, these nanoparticles could be freeze-dried and redispersed in water without a significant change in size. Both DLS and TEM confirmed the formation of nanoparticles with a size of  $\sim 100$  nm. In addition, <sup>1</sup>H NMR analysis confirmed the presence of a new signal at 3.6 ppm and the absence of the aldehyde group at 9.7 ppm attributed to CH<sub>2</sub>O- of the PEG chain and CHO of the aldehyde, respectively (Figure S5). Gel permeation chromatography (GPC) confirmed the increase in molecular weight after the reaction (Figure S6). However, an increase in polydispersity index (PDI) attributed to the differing number of PEG-NH<sub>2</sub> conjugated to the dextran chains was also observed.

The release of dox from the dextran-doxorubicin nanoparticles was investigated under two different pH regimes (pH 7.0 and 5.5). The data in Figure 3 shows dox release over time. At pH 7.0 (corresponding approximately to the pH of blood), dox release was very slow (after 5 days, only 20% of dox had been released from the dextran nanoparticles). In contrast, at pH 5.5 (corresponding to the pH of the early endosome), 70% of dox was released from the PEG aldehyde functionalized

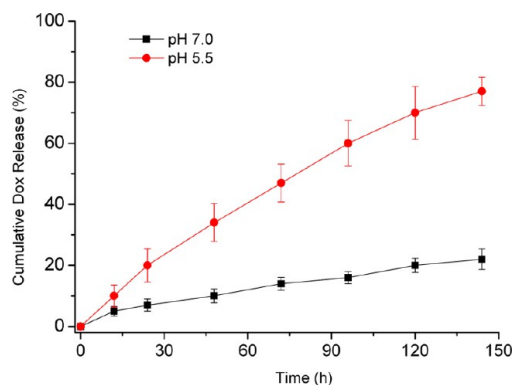
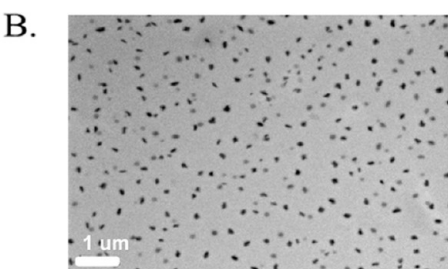


**Figure 3.** Cumulative release of Dox at (red, circle) pH 7.0 and at (dark, square) pH 5.5.



dextran-doxorubicin nanoparticles after 5 days. The integrity of dox after release was confirmed by mass spectroscopy and fluorescence spectroscopy. Electrospray mass spectroscopy confirmed that the molar mass of dox had not changed following release (theoretical mass (dox/H<sup>+</sup>) 544.52, experimental mass (dox/H<sup>+</sup>) 544.18, Figure S7 in the Supporting Information). In addition, the fluorescence spectra characteristic of dox was maintained after release from the dextran nanoparticles (Figure S8 in the Supporting Information). Dox degradation gives rise to new absorption peaks as determined via fluorescence spectroscopy, none of which were observed in the released dox.<sup>38,39</sup>

**Toxicity and Subcellular Distribution of Dextran-Based Nanoparticles in 2D Cell Monolayers.** The biological characterization of two different dextran-based dox delivery systems were examined in this study, a previously reported system in which dox was physically encapsulated into PEG containing acetylated dextran micelles (ac-dex-dox),<sup>18</sup> and the above-described system in which dox was chemically linked via an acid labile bond to PEG containing aldehyde dextran polymers (ald-dex-dox). Initially, toxicity screening was performed in monolayers of two different neuroblastoma cell lines [SH-SY-5Y and SK-N-BE(2)], as well as normal fetal lung fibroblast MRC-5 monolayers. Cell monolayers were exposed to either free dox or the two different dox-loaded dextran nanoparticle systems over an equivalent dox concentration range from 0.001–15  $\mu$ M for 72 h and cell viability was assessed via an Alamar blue assay (Figure S9). For all three cell lines, the physically loaded ac-dex-dox nanoparticles displayed IC<sub>50</sub> closer to free dox, while  $\sim 20$ – $30$ -fold increase in IC<sub>50</sub> against all three cell lines was observed for the chemically linked ald-dex-dox nanoparticles (Table 1). However, it was noted that both the physically loaded ac-dex<sup>18</sup> and chemically linked ald-dex-dox particle (data not shown) systems continued to release their dox load when stored in solution, resulting in reduced efficacy following storage of the particles in solution over the course of a few days. This reduction in efficacy

**Table 1.** IC<sub>50</sub> of Dox, ac-dex-dox, and ald-dex-dox in Multiple Cell Lines As Determined from Regression Analysis of Cell Viability Data

IC <sub>50</sub> ( $\mu$ M)	doxorubicin	ac-dex-dox nanoparticles	ald-dex-dox nanoparticles
SK-N-BE(2)-luc	0.014	0.031	0.298
SH-SY-5Y	0.008	0.01	0.15
MRC-5	0.169	0.469	4.69

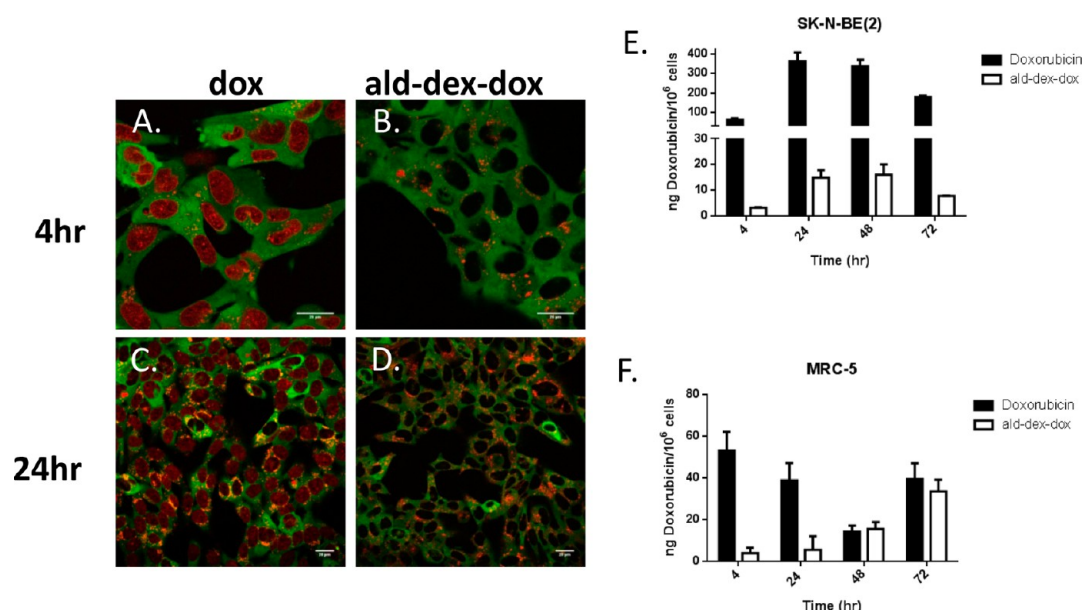


**Figure 4.** Uptake and nuclear localization of (A, C) free dox and (B, D) ald-dex-dox in SK-N-BE(2) cells as visualized by confocal microscopy at (A, B) 4 h and (C, D) 24 h post-incubation. Amount of dox in the nucleus of (E) SK-N-BE(2) cells and (F) MRC-5 cells treated with either free dox or ald-dex-dox over time. Scale bar 20  $\mu$ m; red, dox; green, GFP.

highlighted the necessity of producing a particle formulation capable of being stored in a stable powder form and reconstituted on a per use basis. Unlike the chemically linked ald-dex-dox particle system, attempts to successfully reconstitute the physically loaded ac-dex system from a powder form were unsuccessful as problems arose with inconsistent particle sizing and loss of dox loading. Thus, the majority of further experiments were conducted only with the chemically linked ald-dex-dox system.

The pH responsive nature of dox release from the ald-dex-dox system provides an additional advantage over physically loaded drug delivery systems in that the drug is only released in a low pH environment and, thus, will be preferentially released in the tumor microenvironment or once accumulated into tumor cells. A variety of dox nanocarriers have been developed and in most cases, those designed to physically encapsulate dox tend to show similar or improved efficacy over free dox.<sup>40–42</sup> In contrast, it is not unusual for nanocarriers with dox incorporated via a cleavable, chemical linkage to exhibit an increase in  $IC_{50}$ , similar to what was observed in the ald-dex-dox system.<sup>43,44</sup> The difference in in vitro efficacy has been attributed to differences in dox uptake and release rates from these chemically linked systems.<sup>43</sup> However, nanocarriers such as ald-dex-dox exhibit prolonged circulation times and preferential deposition into tumor tissue and thus, promise greater specificity and enhanced efficacy toward cancer cells in vivo.<sup>9,45</sup>

In addition, the normal MRC-5 cells displayed an even greater reduction in cytotoxicity in response to ald-dex-dox treatment than either the SH-SY-5Y or the SK-N-BE(2) cells as compared to free dox (27-fold vs 18- and 21-fold), indicating a potential enhanced specificity of the ald-dex-dox toward the neuroblastoma cells, which could reduce chemotherapy toxicity to normal cells in vivo.

Doxorubicin's main mechanism of action occurs via DNA intercalation whereby it stabilizes the topoisomerase II complex after it has broken the DNA chain for replication and stops the replication process causing the cells to undergo apoptosis.<sup>46</sup>

Therefore, to further explore the observed difference in  $IC_{50}$  between ald-dex-dox and free dox, subcellular/nuclear localization of dox was examined via confocal microscopy and subcellular fractionation in both the SK-N-BE(2) and MRC-5 cells over time (Figure 4). As expected, live cell confocal microscopy of SK-N-BE(2) cells demonstrated that the majority of free doxorubicin was located in the nucleus of the cells by 4 h post incubation (Figure 4A) and remained in the nucleus at 24 h (Figure 4C). However, 4 h incubation with the ald-dex-dox particles (Figure 4B) resulted in the majority of particle associated dox present in the cytoplasm with little to no dox visible in the nucleus. This subcellular distribution of particle associated dox did not change even after 24 h with the majority still present in the cytoplasm (Figure 4D). Extraction of dox from nuclear fractions of SK-N-BE(2) cells indicated that maximal uptake of free dox into the nucleus occurred at 24–48 h resulting in ~350–400 ng dox/10<sup>6</sup> cells, followed by a decrease at 72 h (Figure 4E). The ald-dex-dox particles showed significantly less dox localizing into the nucleus, with a maximum of less than 20 ng dox/10<sup>6</sup> cells occurring at 48 h. In contrast to the SK-N-BE(2) cells, uptake of free dox into the nucleus of normal MRC-5 fibroblasts peaked at both 24 and 72 h, but at ~10-fold lower maximum nuclear dox concentration than for SK-N-BE(2) cells (Figure 4F). In contrast to what occurs in the SK-N-BE(2) cells, the ald-dex-dox particles showed similar quantities of nuclear localized dox at 48 and 72 h as the free dox in the MRC-5 cells with an increasing trend over time reaching a maximum of ~35 ng/10<sup>6</sup> cells at 72 h.

Despite the almost complete lack of nuclear localization of dox within the ald-dex-dox treated SK-N-BE(2) cells, they still exhibited a significant, albeit reduced cytotoxic response to the ald-dex-dox nanocarriers. Analysis of caspase 3/7 activity (Figure S10) in free dox and ald-dex-dox treated SK-N-BE(2) cells indicated the expected caspase activity in response to free dox treatment, however, no detectable caspase activity was present in cells exposed to ald-dex-dox, even at concentrations shown to produce a cytotoxic effect. Caspases are well-known to be central components of the apoptosis cascade. Caspase 3



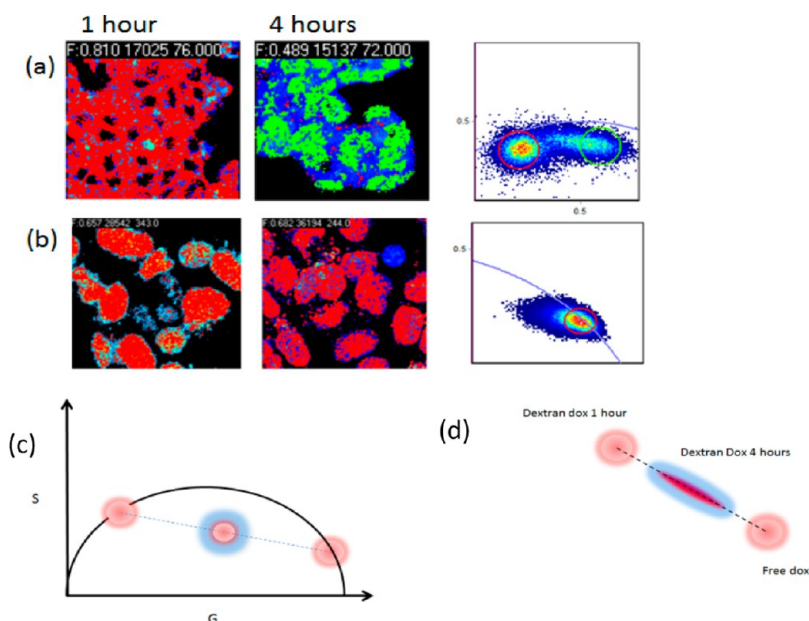


**Figure 5.** Phasor plot analysis of (a) ald-dex-dox and (b) free dox as obtained by fluorescence lifetime imaging microscopy at 1 and 4 h post-uptake in SK-N-BE(2) cells showing a time dependent shift in lifetime between 1 and 4 h for the ald-dex-dox treated cells. (c) All single exponential lifetimes lie on the universal circle while multiexponential lifetimes are a linear combination of their components. (d) The shift in lifetime for the ald-dex-dox treated sample indicates that this is an increase in the fractional contribution of free dox since the points lie in a line between the dextran labeled dox at 1 h and the free dox.

and 7 in particular are known downstream effector caspases responsible for proteolytic cleavage of various cell targets, ultimately leading to cell death. While it is accepted that caspase 3 and 7 are necessary components of the apoptotic cascade, there exists caspase independent mechanisms of cell death.<sup>46</sup> The absence of caspase involvement in response to ald-dex-dox treatment provides strong evidence for a difference in mechanism of action of the ald-dex-dox nanocarriers compared to free dox. This difference in mechanism of action is further supported by the fact that the MRC-5 cells exhibit similar quantities of nuclear localized dox when exposed to either free dox or ald-dex-dox, but significantly different  $IC_{50}$ . To fully elucidate the implication of the differences observed from these results, future experiments will be necessary to explore the mechanistic action of the ald-dex-dox nanocarriers.

**In Vitro Release of Doxorubicin from Aldehyde Dextran Particles.** Due to the low apparent concentrations of dox in the nucleus of cells treated with ald-dex-dox particles, fluorescence lifetime imaging microscopy (FLIM) was employed to confirm successful release of dox from the particles following their uptake into the cells. SK-N-BE(2) cells were incubated with either free dox or ald-dex-dox particles and examined via FLIM at 1 and 4 h post-incubation (Figure 5). The Phasor plot was used to analyze the data recorded using FLIM. The phasor plot<sup>47</sup> provides a model-free assessment of the fluorescence decays, which overcomes some of the problems of exponential fitting fluorescence decays. In FLIM images, the fluorescence decay is fitted at every pixel. In phasor analysis, data is converted into the frequency domain, with fluorescence decays from each pixel represented as sine and cosine Fourier transforms and plotted in a polar plot.<sup>47</sup> All single exponential lifetimes lie on the universal circle while multiexponential lifetimes are a linear combination of their components (Figure 5c).

The inherent fluorescent nature of dox makes it ideal for examining the uptake of dox loaded nanocarriers in vitro.

However, intensity based techniques such as confocal microscopy or flow cytometry are limited in their ability to distinguish between particle associated dox and the drug in its free form as there is little difference between the spectral response of the different drug forms, and as such monitoring drug release in vitro becomes difficult. As an alternative, FLIM has been successfully used in studies involving nanoparticle delivery of dox to elucidate particle associated dox from dox in its free form.<sup>18,48,49</sup> The fluorescence lifetime of a fluorophore is defined as the average time a molecule stays in its excited state before returning to its ground state. This photochemical property of a fluorophore is highly dependent on its physicochemical environment, and as such, is sensitive to factors including but not limited to pH changes, protein binding, and polymer/nanocarrier interactions.<sup>48</sup> Thus, particle associated dox consistently exhibits an increased lifetime over its free form making FLIM ideal for monitoring in vitro drug release from nanocarrier formulations.

The longer lifetime contribution in the phasor plot (highlighted in red) is predominant in the ald-dex-dox sample at 1 h (Figure 5a). From previous characterization it has been established that the dextran labeled dox has a longer fluorescence lifetime than free dox, as shown when comparing lifetimes in the 1 h free dox sample (Figure 5b) with those of the ald-dex-dox sample at 1 h. While no shift in lifetime occurs at 4 h in the free dox sample (Figure 5b), a time-dependent shift in the fluorescence lifetime to a shorter time occurs at 4 h in the ald-dex-dox sample. This shift indicates that this is an increase in the fractional contribution of free dox since the points lie in a line between the dextran-labeled dox at 1 h and the free dox (Figure 5c,d). The FLIM data provides solid evidence to show that the ald-dex-dox particles are being taken up by the cells intact with dox still chemically linked to the particle. Furthermore, the shift in lifetime confirms that dox is in fact being effectively released from the particles following their cellular uptake.

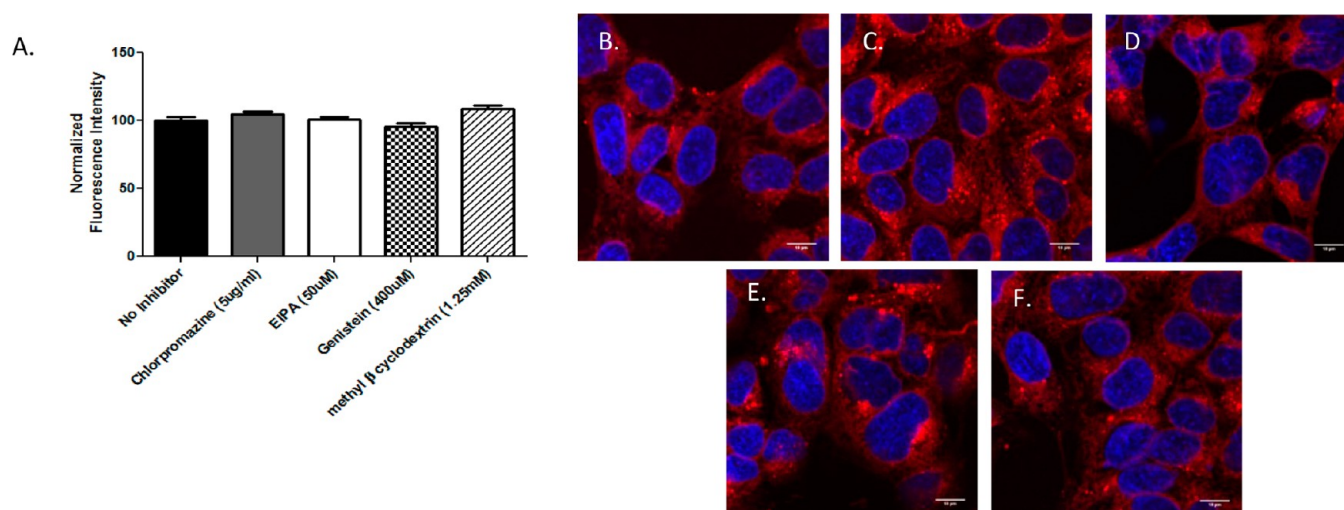


**Figure 6.** Inhibition of clathrin dependent endocytosis, clathrin independent endocytosis, and macropinocytosis of ald-dex-dox nanocarriers in SK-N-BE(2) cells as determined by (A) flow cytometry. Cells were incubated with inhibitors for 2 h followed by incubation with ald-dex-dox for 1 h prior to detection. Confocal microscopy images of SK-N-BE(2) cells incubated for 1 h with ald-dex-dox following 2 h incubation in (B) no inhibitor, (C) chlorpromazine (CDE), (D) methyl- $\beta$ -cyclodextrin (cholesterol depletion, CIE), (E) genistein (CIE), and (F) EIPA (macropinocytosis). Scale bar 10  $\mu$ m; blue, Hoescht 33342; red, ald-dex-dox particles.

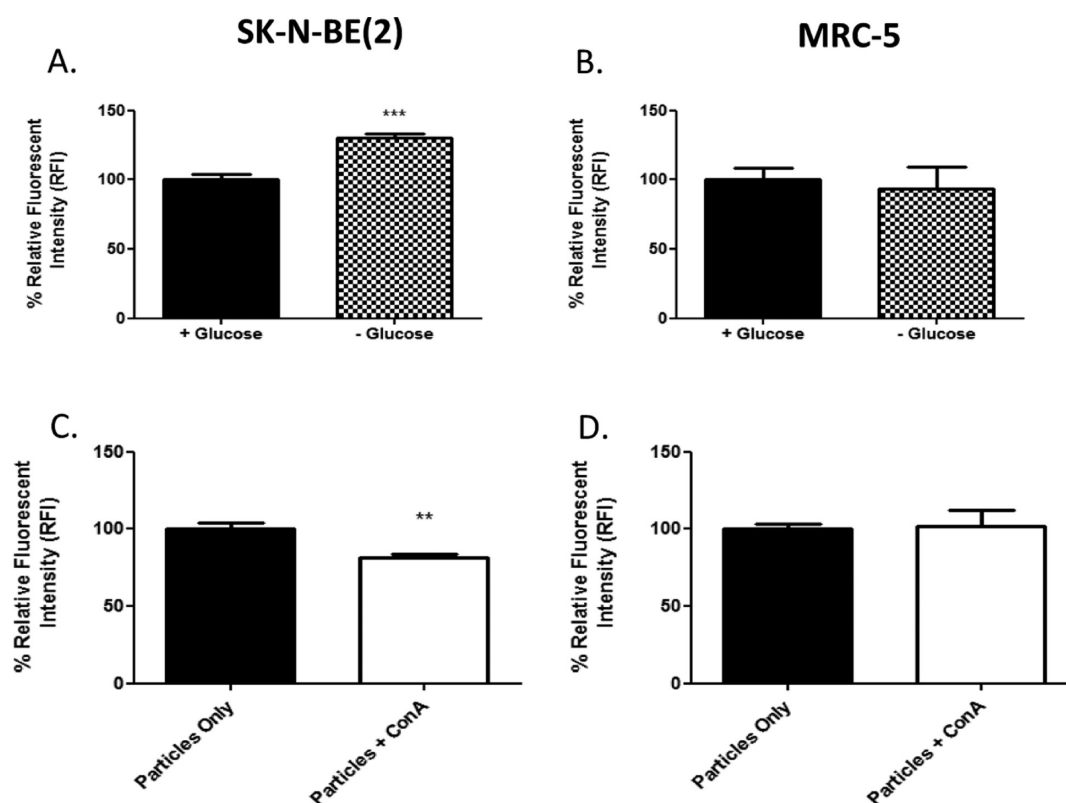


**Figure 7.** Sugar and lectin inhibition of ald-dex-dox uptake. (A) SK-N-BE(2) and (B) MRC-5 grown in glucose containing and glucose free media for 24 h prior to addition of ald-dex-dox for 1 h. (C) SK-N-BE(2) and (D) MRC-5 cells coincubated with conA and ald-dex-dox. Both glucose and conA resulted in a decrease in ald-dex-dox uptake.

**Mechanism of ald-dex-dox Particle Uptake.** To further explore the mechanism of ald-dex-dox nanoparticle internalization and distribution into cells, a range of chemical endocytosis inhibitors were employed, including inhibitors of clathrin-dependent endocytosis (CDE), clathrin-independent endocytosis (CIE), and macropinocytosis. First, inhibitor specificity for the CDE and CIE inhibitors was established in SK-N-BE(2) cells by their ability to block uptake of molecules

known to be internalized via the specific endocytic pathway with minimal toxic effects. In the case of CDE, uptake of human transferrin receptor (hTf), known to be taken up via CDE,<sup>50</sup> was effectively blocked via treatment with chlorpromazine (Figure S11) with little change in cellular morphology and minimal cell death. Lactosylceramide (LacCer) uptake, which is known to be taken up via CIE,<sup>50,51</sup> was effectively inhibited via cholesterol depletion with methyl  $\beta$ -cyclodextrin and the



tyrosine kinase inhibitor genistein (Figure S12). Once the specificity and effectiveness of these particular inhibitors was established, SK-N-BE(2) cells were first exposed to one of the above-mentioned CDE or CIE inhibitors or the well-established macropinocytosis inhibitor EIPA, followed by incubation with ald-dex-dox nanoparticles and examined via both confocal microscopy and flow cytometry (Figure 6). Interestingly, quantitative analysis of ald-dex-dox uptake in response to the individual inhibitors via flow cytometry indicated that none of the aforementioned inhibitors has any significant effect on ald-dex-dox particle uptake, indicating that none of the known major endocytic pathways were responsible for internalization of these particular nanoparticles as visualized via confocal microscopy (Figure 6A). Lack of inhibition was confirmed via confocal microscopy to show the fluorescence signal detected via flow cytometry was not due to particles simply stuck to the outer cell membrane but rather those that were internalized (Figure 6B–F).

Given the above data and the fact that the ald-dex-dox particles are derived from polymers of dextran, the role of these sugars in mediating particle uptake was explored. SK-N-BE(2) and MRC-5 cells were incubated in glucose and nonglucose containing medium for 24 h prior to exposure to ald-dex-dox nanoparticles for 1 h. The absence of glucose in the medium resulted in ~30% increase in ald-dex-dox nanoparticle uptake in the SK-N-BE(2) cells indicating a role for glucose and/or its receptors in the uptake of the ald-dex-dox nanoparticles (Figure 7A). Interestingly, glucose appeared to have little to no effect on particle uptake in MRC-5 cells (Figure 7B). To determine if cell stress due to glucose depletion played a role in altering ald-dex-dox uptake, particles were added in the presence of concanavalin A (ConA), a lectin known to interact with a variety of cell surface sugar moieties and receptors. Approximately a 20% decrease in ald-dex-dox particle uptake in SK-N-BE(2) cells was observed when the particles were added in the presence of ConA (Figure 7C).<sup>52</sup> Similar to the glucose, ConA had little to no effect on ald-dex-dox particle uptake in MRC-5 (Figure 7D).

It has been well established that the specific endocytic pathway responsible for uptake of a nanocarrier can vary greatly and can be dependent on not only cell type, but also the physicochemical properties of the nanocarrier such as size, shape, surface chemistry, and charge, among others.<sup>53</sup> While CDE is the best studied mechanism, several other mechanisms involving molecular regulators have been described and are broadly classified as CIE.<sup>50,53</sup> The most widely studied of the CIE pathways involves caveolin and/or lipid rafts and occurs through a dynamin-dependent process.<sup>53</sup> However, other CIE processes such as Cdc42/Arf1 have been identified and studied, and evidence points to even more as yet described pathways.<sup>50,53,54</sup> Inhibitors of these major CDE and CIE have been used extensively in the literature and are not without their pitfalls,<sup>53,54</sup> however, initial screening of the inhibitors used in this study was performed to ensure inhibitory function in SK-N-BE(2) cells through their ability to block the uptake of LacCer and hTf known to be taken up via CIE and CDE, respectively. In general, the problems associated with endocytosis inhibitors centers around lack of specificity thereby blocking multiple pathways. For instance, methyl- $\beta$ -cyclodextrin is used in studies as a CIE specific inhibitor, however, its mode of action is through the depletion of cholesterol, which can affect CDE and macropinocytosis in addition to CIE.<sup>53,54</sup> Interestingly, none of the inhibitors used were

successful in blocking uptake of ald-dex-dox, thus the problem of lack of specificity was not encountered as none of the most widely studied molecular mechanisms of endocytosis appear to be involved in their uptake. The effectiveness of sugar depletion and the addition of ConA in influencing ald-dex-dox uptake points to a possible role for the cell surface glycocalyx in their uptake into tumor cells. Indeed, aberrant cell surface glycosylation is well characterized in neuroblastoma as well as many other tumor cells, and has been used as a cancer diagnostic marker for many years.<sup>52</sup> It has been suggested that this altered glycosylation could be exploited for not only diagnosis, but also targeted treatment. This has been exemplified in the successful use of an immunotherapy in the treatment of neuroblastoma which specifically targets GD2, a cell surface glycolipid aberrantly expressed in all neuroblastoma tumors.<sup>3</sup> These differences that arise in glycosylation between tumor cells and normal cells could explain the lack of effect of glucose or ConA addition on ald-dex-dox uptake in the normal MRC-5 cells as compared to the inhibitory effect exerted upon the SK-N-BE(2) cells. Further, the differences in the involvement of cell surface glycosylation in ald-dex-dox uptake may be responsible for the greater specificity of the particles toward the neuroblastoma cells as well as the differences observed in nuclear localization of dox.

**Efficacy of ald-dex dox in 3D Tumor Spheroids.** To better mimic the 3D in vivo environment, tumor spheroids of controlled size were generated in a highly reproducible manner from SK-N-BE(2) cells.<sup>34</sup> Tumor spheroids, microscale, self-assembled, spherical clusters of cancer cells, represent one of the simplest 3D models used for drug screening and cancer research. Spheroids larger than 400  $\mu\text{m}$  in diameter will consist of an outer proliferating cell layer and an inner quiescent layer due to limited nutrient and oxygen transport.<sup>55</sup> Neuroblastoma and other tumor cells have been shown to exhibit both morphological and genomic changes when cultured in 3D which better mimic in vivo behavior in comparison to those grown in 2D monolayers.<sup>55–57</sup> Furthermore, the SK-N-BE(2) cell line consists of a heterogeneous population of cells consisting of the three main cell types (I, N, and S type) that when combined with tumor vasculature comprise neuroblastoma tumors in vivo.

In terms of examining the efficacy of drug delivery systems in vitro, spheroids represent a much more physiologically relevant system than 2D monolayers for a variety of reasons. While tumor spheroids cannot perfectly mimic in vivo characteristics as they lack features of the tumor microenvironment such as high interstitial pressure and the presence of microvasculature, they possess a number of biologically relevant characteristics that bridge between in vitro screening and in vivo testing. Of particular relevance to nanocarrier delivery of therapeutics includes the presence of extracellular matrix (ECM) and multicellular arrangements absent from conventional 2D cultures, the existence of multiple cell types and cell–cell interactions comparable to those present in vivo, diffusional limitations, and the presence of cellular microenvironments such as hypoxia.<sup>55</sup> All of these factors can hinder the efficacy of both drug and drug nanocarrier efficacy either by mass transport limitations or by promoting drug resistance via the local microenvironment.

To explore nanoparticle behavior in 3D, SK-N-BE(2) tumor cell spheroids with an average diameter of ~400–500  $\mu\text{m}$  were exposed to either free dox or ald-dex-dox nanoparticles (0.5 and 1  $\mu\text{M}$  equivalent dox) for 24 h. As previously demonstrated,

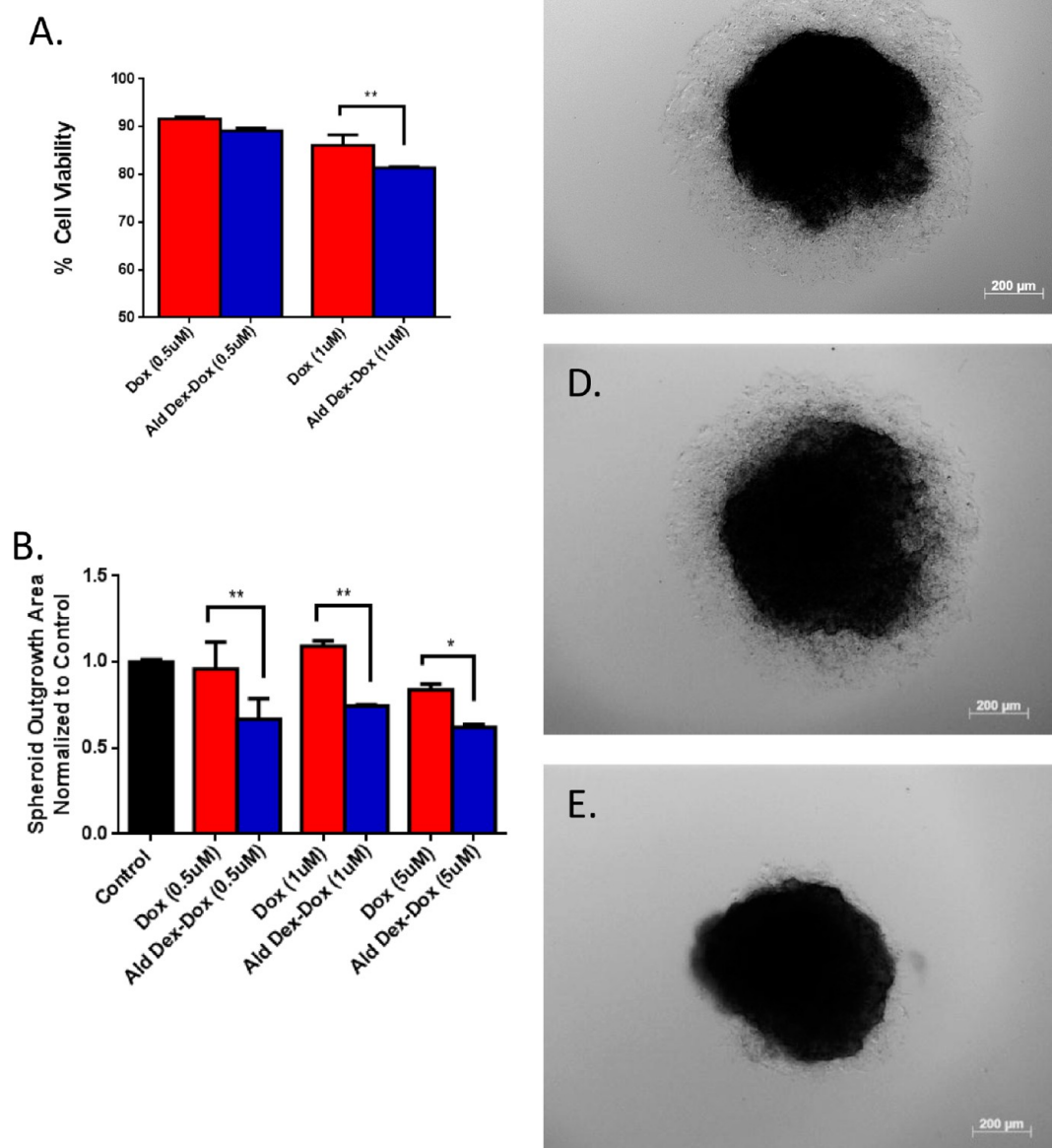


**Figure 8.** Efficacy of free dox and ald-dex-dox 3D spheroid cultures after 24 h exposure to (A) 1  $\mu$ M equivalent dox. Free dox efficacy was greatly reduced in 3D, however, ald-dex-dox showed similar efficacy in 2D and 3D, with a small but significant increase in efficacy in 3D compared to free dox. (B) Spheroid outgrowth was significantly reduced in ald-dex dox treated spheroids at all concentrations examined, while dox treated spheroids demonstrated no reduction in outgrowth when compared to untreated spheroids. Spheroid outgrowth in (C) untreated, (D) 1  $\mu$ M dox, and (E) 1  $\mu$ M ald-dex-dox treated spheroids. Scale bar 200  $\mu$ m.

free dox had significantly improved efficacy over ald-dex-dox nanoparticles in SK-N-BE(2) 2D cell cultures. However, free dox efficacy was greatly reduced in the 3D tumor spheroids with 91 and 86% cell viability after 24 h exposure to 0.5 and 1  $\mu$ M free dox, respectively. Interestingly, cell viability in tumor spheroids exposed to 0.5 and 1  $\mu$ M equivalent ald-dex-dox was almost identical to that observed in monolayers. In fact, efficacy of ald-dex-dox at 1  $\mu$ M dox showed a small yet significant increase in efficacy as compared to 1  $\mu$ M free dox in the 3D spheroids (Figure 8A). As an additional measure of 3D efficacy, spheroid outgrowth was examined in spheroids exposed to free dox or ald-dex-dox nanoparticles (0.5, 1, and 5  $\mu$ M equivalent dox). At all concentrations, spheroids exposed to ald-dex-dox displayed significantly reduced outgrowth as compared to both

the untreated spheroids and those exposed to equivalent free dox concentrations (Figure 8B–D). Additionally, free dox treated spheroids displayed no significant reduction in outgrowth when compared to the untreated spheroids.

The reduced efficacy of chemotherapeutics and, in particular, dox in 3D versus 2D systems has been well documented.<sup>55,57–59</sup> Thus, the decrease in efficacy of free dox in the 3D tumor spheroids was to be expected. Generally, a similar trend is seen for nanocarrier systems in both 3D in vitro systems as well as in vivo, which has been attributed to some extent to a limited ability to penetrate deeply into solid tumors.

**Penetration of ald-dex-dox Particles into 3D Tumor Spheroids.** SK-N-BE(2) tumor spheroids  $\sim$ 400–500  $\mu$ m in diameter were exposed to free dox and monitored over time via

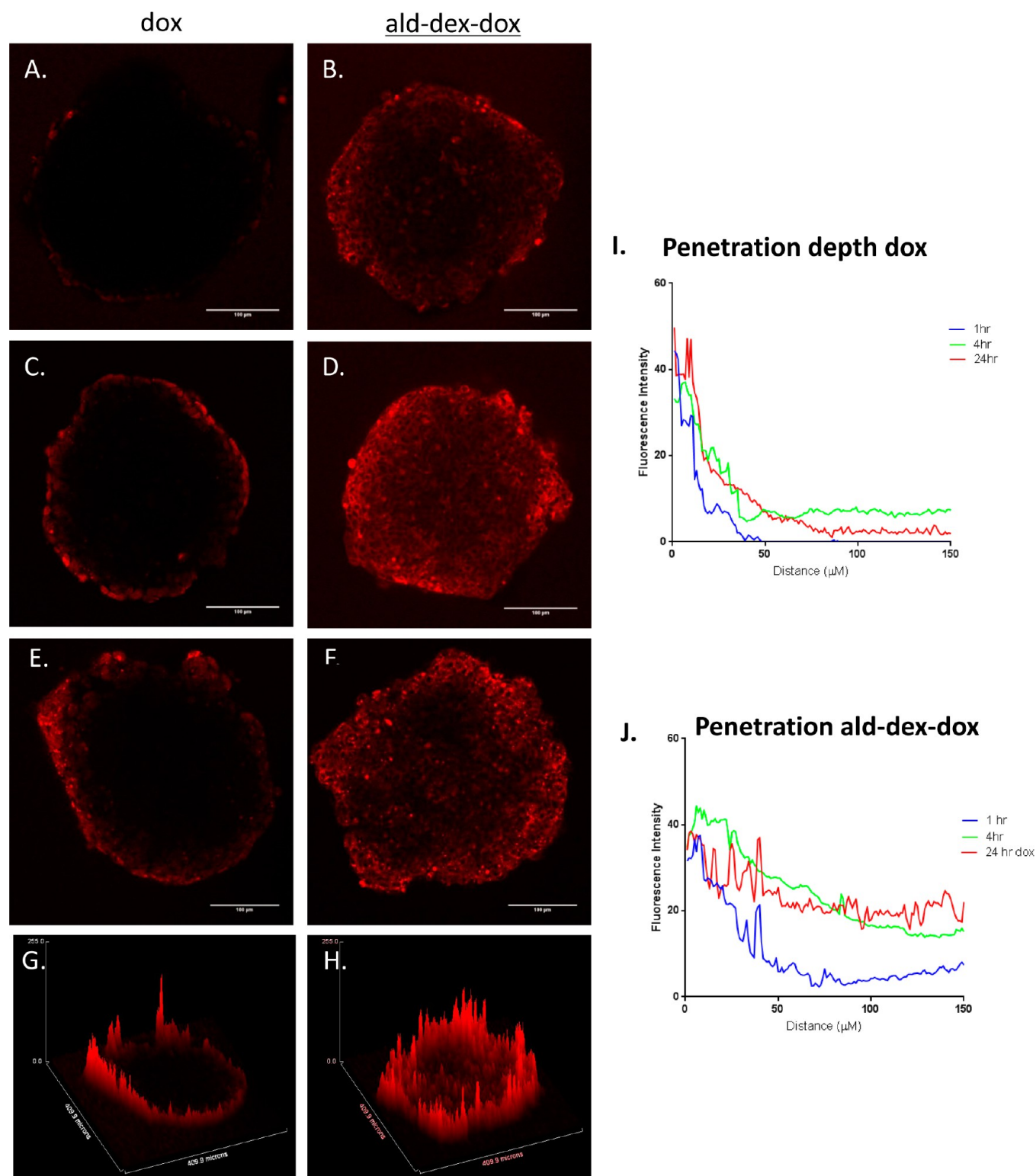


**Figure 9.** Drug penetration into tumor spheroids after (A, B) 1 h, (C, D) 4 h, (E, F) or 24 h exposure to either (A, C, E) free dox or (B, D, F) ald-dex-dox. Free dox reaches a maximal penetration depth of  $\sim 50 \mu\text{m}$  from the edge of the spheroid, while after only 4 h, ald-dex-dox has fully penetrated into the center of the spheroid. Scale bar  $100 \mu\text{m}$ . (G, H) Surface plots of images E and F, respectively, produced in image J. (I, J) Fluorescent intensity profiles calculated across the spheroids from the spheroid edge at 1, 4, and 24 h of dox and ald-dex-dox penetration (obtained by analysis of 5–6 different spheroids for each treatment and each time point). Two-way ANOVA analysis of penetration curves indicates a significant difference between penetration depth of ald-dex-dox and dox at all three time points.

confocal microscopy to assess the ability of the drug to penetrate into the 3D structure (Figure 9). As previously reported, maximum penetration was reached at 24 h (Figure

9E,G), at which time, dox had penetrated  $\sim 50 \mu\text{m}$  into the spheroid.<sup>55,60</sup> Longer incubation time had no effect on further penetration of the drug into the spheroid (data not shown).



Unexpectedly, ald-dex-dox nanoparticle had already penetrated the tumor spheroids to a distance of 50  $\mu\text{m}$  after 1 h (Figure 9B), with full penetration of the spheroid at 4 h (Figure 9D). Full penetration of the ald-dex-dox nanoparticles was maintained over longer time periods (Figure 9F,H). Further demonstration of the enhanced ald-dex-dox penetration can be seen in fluorescence intensity (FI) profiles calculated across the spheroids from the spheroid edge at 1, 4, and 24 h (Figure 9I,J). The FI of dox exhibits a rapid decrease to background levels indicating little to no dox penetration past 50  $\mu\text{m}$ , while ald-dex-dox displays a consistent FI profile at both 4 and 24 h, indicating full penetration. Unlike the ald-dex-dox nanoparticles, the physically loaded Ac-Dex nanoparticles were unable to effectively penetrate into the tumor spheroids (Figure S13), as is typical for most nanoparticle systems, thus, demonstrating the unique behavior of the ald-dex-dox delivery system.<sup>20,24,45,61</sup>

The problem of limited penetration depth of nanocarriers into the extravascular space of tumors has only recently begun to be addressed, albeit, with limited success.<sup>6,7,10,20</sup> The majority of studies involving nanocarrier delivery of therapeutics conducted rely heavily on the EPR effect when discussing translation of the *in vitro* results obtained to *in vivo* efficacy. However, the traditional view of the EPR is a highly simplified version of the actual tumor microenvironment, and it is vital that these additional barriers preventing *in vivo* success, such as limited penetration and access to tumor cells, receive significantly more attention.<sup>6,10</sup> One strategy that has exhibited some success in overcoming limited penetration depth involves the inclusion of the tissue penetrating peptide iRGD, which acts as both a tumor targeting moiety while concurrently enhancing tumor tissue penetration.<sup>6,10,20,24</sup> Another strategy has targeted the dense ECM often associated with solid tumors by codelivery of enzymes, which can assist in breaking down the ECM thereby improving mass transport within the tissue.<sup>24,29,30</sup> Other studies have pointed to a minimal particle size of less than 100 nm and a specific shape as a necessity for nanocarrier penetration.<sup>27,30,62</sup> And still others have indicated the necessity of surface charge in the absence of peptides or enzymes.<sup>9,10,24,28</sup> Despite these limited successes, there is still a gap in understanding the nanomaterial structure/function relationship necessary for promoting tumor penetration. The ald-dex-dox nanocarriers are nonionic particles with an average size greater than 100 nm and, thus, do not appear to possess any of the commonly reported characteristics necessary for penetration. The ability of these particles to exhibit such enhanced penetration ability within the tumor spheroids is highly unique both in terms of their size and their lack of known physicochemical properties known for enhancing penetration. Given the suggested role of the glycocalyx in the uptake of these particles in tumor cells, it is likely interactions between cell surface glycolipids/glycoproteins and the ald-dex-dox results in the nanocarriers effectively moving between the tight cell–cell junctions, thereby penetrating into the spheroids. Interestingly, given the lack of penetration of the acetylated dextran nanoparticles, the inclusion of dextran alone is not sufficient for promoting enhanced nanoparticle penetration. The difference between two similar dextran-based systems points toward a specificity in conformation/arrangement of the dextran polymers that may allow the dextran within the ald-dex-dox to specifically interact with the cell surface as being responsible for the unique behavior of the ald-dex-dox nanocarriers. Dhanikula et al. demonstrated that glucosamine

modification of dendrimers effectively enhanced their ability to penetrate avascular glioma tumor spheroids.<sup>63</sup> It was suggested that the glucosamine, accessible on the particle surface, could interact with glucose transporters and thus the ability of the glucosamine modified dendrimers to penetrate into avascular spheroids was due to the hypoxia related increase in glucose transport.<sup>63</sup> While the specific interactions occurring between the ald-dex-dox and the cell glycocalyx have not yet been elucidated, the enhanced penetration and efficacy in 3D is likely a direct result of a specific interaction between the dextran polymer and the highly glycosylated tumor cell surface. The results from this study combined with that of the aforementioned study involving glucosamine modification point toward the possibility of exploiting carbohydrate chemistries in the development of nonionic nanocarriers with enhanced penetration ability for enhanced cancer treatments.

## ■ CONCLUSIONS

The current study has demonstrated the ability of a neutral, dextran based dox nanocarrier to effectively penetrate into 3D tumor spheroids. dox, along with other commonly used chemotherapeutics suffer from limited drug penetration *in vivo*, which can result in ineffective treatments due to exposure of cells to sublethal drug concentrations and ultimately lead to the development of drug resistance.<sup>64</sup> Nanocarriers suffer to an even greater extent from low tissue penetration depths, thus despite the advantages they provide in terms of improved pharmacokinetics and reduced systemic exposure, enhanced *in vivo* efficacy is often lacking. Thus, nanoparticle studies performed in 2D monolayers rarely translate to *in vivo* results, highlighting the necessity of employing more complex 3D *in vitro* models when prescreening nanocarrier systems. This fact is exemplified with the ald-dex-dox nanocarriers characterized in this study which shows poor efficacy in 2D monolayers when compared to the parent drug, but outperformed the free Dox when examined in a more biologically relevant 3D tumor spheroid model.

The enhanced 3D efficacy can be attributed to the unique ability of these nanocarriers to fully penetrate into the tumor tissue. Thus, given the promising *in vitro* 3D results for the ald-dex-dox system, future studies will aim to explore the efficacy and penetration ability of these nanocarriers *in vivo*. Few (if any studies) to date have demonstrated the ability of neutrally charged nanocarriers over  $\sim 60$  nm in diameter to penetrate tumor tissue without the aid of codelivered enzymes or targeting moieties with tissue penetrating abilities.<sup>6,7,24,26,65</sup> Given the suggested role of the glycocalyx in the uptake of the ald-dex-dox nanoparticles, the interactions between this dextran based nanocarrier and the highly glycosylated tumor cell surface may provide clues to their penetration ability. This study provides an important step toward understanding chemical modifications, which could assist in improving nanocarrier penetration into tumor tissue, thereby enhancing their efficacy.

## ■ ASSOCIATED CONTENT

### Supporting Information

Graphs of the cytotoxicity profile of free dox, ald-dex, and ac-dex in SK-N-BE(2), SH-SY-SY, and MRC-5 cells. The activity of caspase 3/7 in response to both free dox and ald-dex-dox treatment is also included. Confocal microscopy images demonstrating specificity and efficacy of endocytic inhibitors as well as an image of ac-dex nanoparticle penetration into 3D

spheroids are additionally included. This material is available free of charge via the Internet at <http://pubs.acs.org>.

## AUTHOR INFORMATION

### Corresponding Author

\*Phone: +61 2 9385 2151. E-mail: [m.kavallaris@ccia.unsw.edu.au](mailto:m.kavallaris@ccia.unsw.edu.au). Fax: +61 2 9662 6583.

### Notes

The authors declare no competing financial interest.

## ACKNOWLEDGMENTS

This work was supported by the Children's Cancer Institute Australia for Medical Research, which is affiliated with the University of New South Wales and Sydney Children's Hospital and by the Balnaves Foundation Young Investigator Grant (S.M.S.), National Health and Medical Research Council Grant (NHMRC APP1008719; M.K. and J.A.M.), Cancer Council New South Wales Program Grant (M.K.), Cancer Institute New South Wales Career Development Fellowship (J.A.M.), and NHMRC Senior Research Fellowship (M.K.; #658611). C.B. is the recipient of an Australian Postdoctoral Award (ARC-DP1092640) and Future Fellow Fellowship (ARC-FT 120100096) from the Australian Research Council. The authors thank the Nuclear Magnetic Resonance Facility, Biomedical Imaging Facility, and the Electron Microscope Unit at the Mark Wainwright Analytical Centre, University of New South Wales.

## REFERENCES

- Gutierrez, J. C.; Fischer, A. C.; Sola, J. E.; Perez, E. A.; Koniaris, L. G. *Pediatr. Surg. Int.* **2007**, *23*, 637–646.
- Maris, J. M. *New Engl. J. Med.* **2010**, *362*, 2202–2211.
- Sondel, P. M.; Yang, R. K. *Drug Future* **2010**, *35*, 665–673.
- Ara, T.; DeClerck, Y. A. *Cancer Metast. Rev.* **2006**, *25*, 645–657.
- Perwein, T.; Lackner, H.; Sovinz, P.; Benesch, M.; Schmidt, S.; Schwinger, W.; Urban, C. *Pediatr. Blood Cancer* **2011**, *57*, 629–635.
- Ruoslahti, E.; Bhatia, S. N.; Sailor, M. J. *J. Cell Biol.* **2010**, *188*, 759–768.
- Sugahara, K. N.; Teesalu, T.; Karmali, P. P.; Kotamraju, V. R.; Agemy, L.; Girard, O. M.; Hanahan, D.; Mattrey, R. F.; Ruoslahti, E. *Cancer Cell* **2009**, *16*, 510–520.
- Farrell, D.; Ptak, K.; Panaro, N. J.; Grodzinski, P. *Pharm. Res.* **2011**, *28*, 273–278.
- Lammers, T.; Hennink, W. E.; Storm, G. *Br. J. Cancer* **2008**, *99*, 392–397.
- Lammers, T.; Kiessling, F.; Hennink, W. E.; Storm, G. *J. Controlled Release* **2012**, *161*, 175–187.
- Bachelder, E. M.; Beaudette, T. T.; Broaders, K. E.; Dashe, J.; Frechet, J. M. J. *J. Am. Chem. Soc.* **2008**, *130*, 10494–+.
- Bisht, S.; Maitra, A. *Wiley Interdiscip. Rev.: Nanomed. Nanobiotechnol.* **2009**, *1*, 415–425.
- Broaders, K. E.; Cohen, J. A.; Beaudette, T. T.; Bachelder, E. M.; Frechet, J. M. J. *Proc. Natl. Acad. Sci. U.S.A.* **2009**, *106*, 5497–5502.
- Li, Y. L.; Zhu, L.; Liu, Z. Z.; Cheng, R.; Meng, F. H.; Cui, J. H.; Ji, S. J.; Zhong, Z. Y. *Angew. Chem., Int. Ed.* **2009**, *48*, 9914–9918.
- Verma, M. S.; Liu, S. Y.; Chen, Y. Y.; Meerasa, A.; Gu, F. X. *Nano Res.* **2012**, *5*, 49–61.
- Saptarshi, S. R.; Duschl, A.; Lopata, A. L. *J. Nanobiotechnol.* **2013**, *11*.
- Jeong, Y. I.; Chung, K. D.; Choi, K. H. *Arch. Pharmacol. Res.* **2011**, *34*, 159–167.
- Duong, H. T. T.; Marquis, C. P.; Whittaker, M.; Davis, T. P.; Boyer, C. *Macromolecules* **2011**, *44*, 8008–8019.
- Jeong, Y. I.; Kim, D. H.; Chung, C. W.; Yoo, J. J.; Choi, K. H.; Kim, C. H.; Ha, S. H.; Kang, D. H. *Int. J. Nanomed.* **2011**, *6*, 1415–1427.
- Feron, O. *Sci. Transl. Med.* **2010**, *2*, 1–5.
- Lee, P. Y.; Wong, K. K. Y. *Curr. Drug Delivery* **2011**, *8*, 245–253.
- Wang, Y. C.; Brown, P.; Xia, Y. N. *Nat. Mater.* **2011**, *10*, 482–483.
- Raha, S.; Paunesku, T.; Woloschak, G. *Wiley Interdiscip. Rev.: Nanomed. Nanobiotechnol.* **2011**, *3*, 269–281.
- Holback, H.; Yeo, Y. *Pharm. Res.* **2011**, *28*, 1819–1830.
- Sagnella, S. M.; Gong, X. J.; Moghaddam, M. J.; Conn, C. E.; Kimpton, K.; Waddington, L. J.; Krodziewska, I.; Drummond, C. J. *Nanoscale* **2011**, *3*, 919–924.
- Wong, C.; Stylianopoulos, T.; Cui, J. A.; Martin, J.; Chauhan, V. P.; Jiang, W.; Popovic, Z.; Jain, R. K.; Bawendi, M. G.; Fukumura, D. *Proc. Natl. Acad. Sci. U.S.A.* **2011**, *108*, 2426–2431.
- Chauhan, V. P.; Popovic, Z.; Chen, O.; Cui, J.; Fukumura, D.; Bawendi, M. G.; Jain, R. K. *Angew. Chem., Int. Ed.* **2011**, *50*, 11417–11420.
- Meng, H.; Xue, M.; Xia, T.; Ji, Z. X.; Tarn, D. Y.; Zink, J. I.; Nel, A. E. *ACS Nano* **2011**, *5*, 4131–4144.
- Liu, Q.; Li, R. T.; Qian, H. Q.; Yang, M.; Zhu, Z. S.; Wu, W.; Qian, X. P.; Yu, L. X.; Jiang, X. Q.; Liu, B. R. *Int. J. Nanomed.* **2012**, *7*, 281–295.
- Goodman, T. T.; Olive, P. L.; Pun, S. H. *Int. J. Nanomed.* **2007**, *2*, 265–274.
- Bernstein, A.; Hurwitz, E.; Maron, R.; Arnon, R.; Sela, M.; Wilchek, M. *J. Natl. Cancer I* **1978**, *60*, 379–384.
- Ortiz, R.; Au, J. L. S.; Lu, Z.; Gan, Y.; Wientjes, M. G. *AAPS J.* **2007**, *9*, E241–E250.
- Byrne, F. L.; Yang, L.; Phillips, P. A.; Hansford, L. M.; Fletcher, J. I.; Ormandy, C. J.; McCarroll, J. A.; Kavallaris, M. *Oncogene* **2013**, DOI: 10.1038/onc.2013.11.
- Vinci, M.; Gowan, S.; Boxall, F.; Patterson, L.; Zimmermann, M.; Court, W.; Lomas, C.; Mendiola, M.; Hardisson, D.; Eccles, S. A. *BMC Biol.* **2012**, *10*, 10–29.
- Heinze, T.; Liebert, T.; Heublein, B.; Hornig, S. In *Polysaccharides II*; Klemm, D., Ed.; Springer-Verlag: Berlin, 2006; Vol. 205, pp 199–291.
- Mehvar, R. *J. Controlled Release* **2000**, *69*, 1–25.
- Naeye, B.; Raemdonck, K.; Remaut, K.; Sproat, B.; Demeester, J.; De Smedt, S. C. *Eur. J. Pharm. Sci.* **2010**, *40*, 342–351.
- Beijnen, J. H.; van der Houwen, O. A. G. J.; Underberg, W. J. M. *Int. J. Pharm.* **1986**, *32*, 123–131.
- Barenholz, Y.; Amselem, S.; Goren, D.; Cohen, R.; Gelvan, D.; Samuni, A.; Golden, E. B.; Gabizon, A. *Med. Res. Rev.* **1993**, *13*, 449–491.
- Goren, D.; Horowitz, A. T.; Tzemach, D.; Tarshish, M.; Zalipsky, S.; Gabizon, A. *Clin. Cancer Res.* **2000**, *6*, 1949–1957.
- Jung, S.; Jeong, Y. I.; Jin, S. G.; Kim, I. Y.; Pei, J.; Wen, M.; Jung, T. Y.; Moon, K. S. *Colloids Surf., B* **2010**, *79*, 149–155.
- Kim, D.; Gao, Z. G.; Lee, E. S.; Bae, Y. H. *Mol. Pharmaceutics* **2009**, *6*, 1353–1362.
- Shi, M.; Ho, K.; Keating, A.; Shoichet, M. S. *Adv. Funct. Mater.* **2009**, *19*, 1689–1696.
- Xu, R. Z.; Fisher, M.; Juliano, R. L. *Bioconjugate Chem.* **2011**, *22*, 870–878.
- Jain, R. K.; Stylianopoulos, T. *Nat. Rev. Clin. Oncol.* **2010**, *7*, 653–664.
- Swift, L. P.; Rephaeli, A.; Nudelman, A.; Phillips, D. R.; Cutts, S. M. *Cancer Res.* **2006**, *66*, 4863–4871.
- Digman, M. A.; Caiola, V. R.; Zama, M.; Gratton, E. *Biophys. J.* **2008**, *94*, L14–L16.
- Dai, X. W.; Yue, Z. L.; Eccleston, M. E.; Swartling, J.; Slater, N. K. H.; Kaminski, C. F. *Nanomed. Nanotechnol.* **2008**, *4*, 49–56.
- Wang, Y. L.; Newell, B. B.; Irudayaraj, J. *J. Biomed. Nanotechnol.* **2012**, *8*, 751–759.
- Vercauteren, D.; Vandenbroucke, R. E.; Jones, A. T.; Reijman, J.; Demeester, J.; De Smedt, S. C.; Sanders, N. N.; Braeckmans, K. *Mol. Ther.* **2010**, *18*, 561–569.
- Khalil, I. A.; Kogure, K.; Akita, H.; Harashima, H. *Pharmacol. Rev.* **2006**, *58*, 32–45.

- (52) Drake, P. M.; Cho, W.; Li, B. S.; Prakobphol, A.; Johansen, E.; Anderson, N. L.; Regnier, F. E.; Gibson, B. W.; Fisher, S. J. *Clin. Chem.* **2010**, *56*, 223–236.
- (53) Iversen, T. G.; Skotland, T.; Sandvig, K. *Nano Today* **2011**, *6*, 176–185.
- (54) Ivanov, A. I. *Method Mol. Biol.* **2008**, *440*, 15–33.
- (55) Mehta, G.; Hsiao, A. Y.; Ingram, M.; Luker, G. D.; Takayama, S. *J. Controlled Release* **2012**, *164*, 192–204.
- (56) Li, G. N.; Livi, L. L.; Gourd, C. M.; Deweerd, E. S.; Hoffman-Kim, D. *Tissue Eng.* **2007**, *13*, 1035–1047.
- (57) Loessner, D.; Stok, K. S.; Lutolf, M. P.; Hutmacher, D. W.; Clements, J. A.; Rizzi, S. C. *Biomaterials* **2010**, *31*, 8494–8506.
- (58) Dufau, I.; Frongia, C.; Sicard, F.; Dedieu, L.; Cordelier, P.; Ausseil, F.; Ducommun, B.; Valette, A. *BMC Cancer* **2012**, *12*, 12–15.
- (59) Frieboes, H. B.; Edgerton, M. E.; Fruehauf, J. P.; Rose, F. R. A. J.; Worrall, L. K.; Gatenby, R. A.; Ferrari, M.; Cristini, V. *Cancer Res.* **2009**, *69*, 4484–4492.
- (60) Primeau, A. J.; Rendon, A.; Hedley, D.; Lilge, L.; Tannock, I. F. *Clin. Cancer Res.* **2005**, *11*, 8782–8788.
- (61) Ding, D.; Zhu, Z. S.; Liu, Q.; Wang, J.; Hu, Y.; Jiang, X. Q.; Liu, B. R. *Eur. J. Pharm. Biopharm.* **2011**, *79*, 142–149.
- (62) Huang, K. Y.; Ma, H. L.; Liu, J.; Huo, S. D.; Kumar, A.; Wei, T.; Zhang, X.; Jin, S. B.; Gan, Y. L.; Wang, P. C.; He, S. T.; Zhang, X. N.; Liang, X. J. *ACS Nano* **2012**, *6*, 4483–4493.
- (63) Dhanikula, R. S.; Argaw, A.; Bouchard, J. F.; Hildgen, P. *Mol. Pharmaceutics* **2008**, *5*, 105–116.
- (64) Tannock, I. F.; Lee, C. M.; Tunggal, J. K.; Cowan, D. S. M.; Egorin, M. J. *Clin. Cancer Res.* **2002**, *8*, 878–884.
- (65) Sugahara, K. N.; Teesalu, T.; Karmali, P. P.; Kotamraju, V. R.; Agemy, L.; Greenwald, D. R.; Ruoslahti, E. *Science* **2010**, *328*, 1031–1035.